Applied Mathematical Modelling 54 (2018) 752–767

Contents lists available at ScienceDirect

Applied Mathematical Modelling

journal homepage: www.elsevier.com/locate/apm

Very high-order accurate finite volume scheme on curved boundaries for the two-dimensional steady-state convection–diffusion equation with Dirichlet condition

Ricardo Costa [a,b], Stéphane Clain [b,*], Raphaël Loubère [c], Gaspar J. Machado [b]

[a] Institut de Mathématiques de Toulouse, Université Paul Sabatier, 31062 Toulouse, France
[b] Centro de Matemática, Universidade do Minho, Campus de Azurém, 4800-058 Guimarães, Portugal
[c] CNRS DR researcher, University of Bordeaux Mathematical Institute of Bordeaux (IMB), 33405 Talence, France

ARTICLE INFO

Article history:
Received 23 November 2016
Revised 10 October 2017
Accepted 11 October 2017
Available online 23 October 2017

Keywords:
Very high-order finite volume method
Curved boundaries
Reconstruction for Off-site Data (ROD)

ABSTRACT

Accuracy may be dramatically reduced when the boundary domain is curved and numerical schemes require a specific treatment of the boundary condition to preserve the optimal order. In the finite volume context, Ollivier-Gooch and Van Altena (2002) has proposed a technique to overcome such limitation and restore the very high-order accuracy which consists in specific restrictions considered in the least-squares minimization associated to the polynomial reconstruction. The method suffers from several drawbacks, particularly, the use of curved elements that requires sophisticated meshing algorithms. We propose a new method where the physical domain and the computational domain are distinct and we introduce the Reconstruction for Off-site Data (ROD) where polynomial reconstructions are carried out on the mesh using data localized outside of the computational domain, namely the Dirichlet condition situated on the physical domain. A series of numerical tests assess the accuracy, convergence rates, robustness, and efficiency of the new method and show that the boundary condition is fully integrated in the scheme with a very high-order accuracy and the optimal convergence rate is achieved.

1. Introduction

Very high-order finite volume methods require supplemental attention to achieve the optimal order. One of the major difficulties is the boundary treatment when dealing with curved boundary domains, since polygonal meshes do not exactly fit the physical domain. Without special attention we observe a dramatic reduction of the accuracy and the method turns out to be a second-order accurate one [1,2]. Reaching the nominal convergence order of very high-order methods then requires additional efforts and is of paramount importance nowadays [3,4]. Several critical issues motivate the use of very high-order approximations with curved boundaries. For the Euler system, it is difficult to compute asymptotic solutions when using piecewise linear approximations of the geometries [5] even for very fine meshes. Moreover, non-physical approximations may be obtained when curved boundaries are substituted with piecewise linear straight lines [1,2].

* Corresponding author.
E-mail addresses: rcosta@math.univ-toulouse.fr (R. Costa), clain@math.uminho.pt (S. Clain), raphael.loubere@u-bordeaux.fr (R. Loubère), gjm@math.uminho.pt (G.J. Machado).

https://doi.org/10.1016/j.apm.2017.10.016
0307-904X/

Several technologies to recover the optimal order have then been proposed and extensively tested. Deriving from the Finite Element approach [6–9], the Discontinuous Galerkin method [10,11] handles curved boundaries with isoparametric elements first introduced by Bassi and Rebay [1]. A similar approach has also been developed for the Spectral Volume method [4,12]. In short, the technology is based on two major ingredients: the mesh considers curved elements such that the boundary of the computational domain fits with the physical boundary (at least up to a given error $O(h^k)$) and the introduction of nonlinear transformations to map the curved elements to the reference one.

The method is efficient and provides optimal order of convergence but suffers from several drawbacks. The element mapping introduces the Jacobian transformations in the volume and interface integrals that are evaluated in the local basis (the reference element coordinates). Such expressions become cumbersome when dealing with high polynomial degrees and lead to an additional computational effort. Moreover a change of sign of the Jacobian mapping, *i.e.* folded or tangled elements, may occur and disqualifies the transformation [13,14]. The second and more critical drawback is the meshing procedure with curved elements, that reveals impractical for complex geometries especially for three-dimension configurations [2]. Curved mesh generation is a today's challenge [3] and is far from being completely solved [15]. Meshing very complex geometries with unstructured hybrid grids has still not reached the level of commercial grid generators.

Alternative methods have been then proposed to avoid the nonlinear mapping and the curved mesh generation.

- In [2], the authors use the computational polygonal domain in place of the physical domain but modify the normal vector involved in the wall boundary condition (see also [16]). Accuracy improvement is obtained but, unfortunately, the method has only been tested with quadratic boundaries and seems to be, at most, a third-order approximation since it considers local curvature approximations, *i.e.* second derivatives in the Taylor expansion.
- Another promising method is the so-called "Extensions from Subdomains" introduced in [17–19]. The idea is to derive a new Dirichlet condition on the computational domain edge from the one evaluated on the physical boundary. An additional contribution is obtained from the integration of the solution over a path linking points x_{comp} and x_{phys} lying on their respective borders. The main advantage is that no local mapping or curved element is required but an extension of the numerical approximation has to be evaluated in order to perform the integration of the approximation gradient outside the computational domain. Unfortunately, the method is only available for second-order operators with diffusion or viscosity term. The second drawback is the necessity to define path families between the edges of the computational mesh boundary and the physical one. Such procedure introduces constrained local minimization operations to define local one-to-one mappings $x \to a(x)$ from the boundary edges and the associated pieces of the physical boundary. Then, the paths are derived from linear interpolation $[x, a(x)]$. At last, numerical integrations over the paths are required to compute the additional contributions to update the associate Dirichlet condition on the computational boundary.
- We also mention the unfitted Finite Element method where an inner interface corresponding to a change of material properties does not fit with the mesh [20]. Two linear reconstructions are considered in the same cell where the interface is localized (one for each side). Then a specific weak formulation is derived taking into account the inner interface while flux conservation and continuity is assume to solve the problem. Extension for higer order finite elements is considered in [21] where a local transformation, very similar to the isoparametric one, is considered to fit a local discretized interface with the physical one using the isoparametric transformation proposed in [22]. The main drawback of the method is the use of isoparametric transformation that involves more complex algebra and additional computational costs.
- In the context of the finite volume method involving k-exact polynomial reconstructions, the pioneer work of Ollivier-Gooch and Van Altena [23] gives rise to a very high-order finite volume method dealing with curved boundary for the convection–diffusion equation and Euler and Navier–Stokes systems [24–26]. The method does not require any geometrical transformation but the mesh has to be composed with curved cells that fits the physical boundary. Likewise for the Discontinuous Galerkin method, it represents a severe drawback due to the difficulties to provide such curved elements for complex geometries. Moreover, the method suffers from other problems. Indeed, one has to perform numerical integrations over the curved elements to evaluate any source term or the initial condition mean-values and on the curved boundaries to calculate the numerical fluxes. Integration on a piece of curves boundary for the two-dimensional situation requires an extra-effort for localizing the Gauss points, but the problem turns out to be cumbersome when dealing with a three-dimensional domain [27]. Integration over the cell is a major difficulty. Indeed, while Gaussian points are well-located for simple geometries, it seems almost impossible to derive numerical quadratures rules for generic curved element except for special situations such as pieces of circles or spheres [25].

We propose a new and simple treatment of Dirichlet conditions in the context of very high-order finite volume methods with a curved boundary domain. Because this paper is a proof of concept, we choose the simplest situation, namely the steady-state convection–diffusion with Dirichlet condition on two-dimensional curved domains. Extensions such as three-dimensional geometries, Neumann or mixed condition, and non-stationary systems will be considered in the future.

As in [17,27], we consider two distinct regions: the physical domain, where the continuous problem takes place, and the computational polygonal domain, where the discretization is designed and the numerical solution is evaluated. Obviously, Dirichlet conditions prescribed on the physical boundary have to be transferred in some way to the computational domain. The corner-stone of our work is the design of a specific polynomial reconstruction that takes the real boundary condition into account. Therefore we perform a reconstruction with data that are not all localized on the mesh and name the method "Reconstruction for Off-site Data" with acronym "ROD" to highlight that data are not supported by the computational domain.

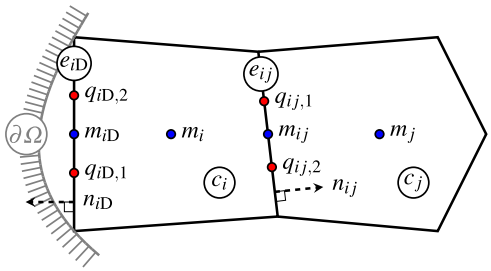

Fig. 1. Mesh notation with edge and cell reference points (blue dots), Gauss points (red dots associated to a two-point quadrature rule), and unit normal vectors (dashed lines). (For interpretation of the references to color in this figure legend, the reader is referred to the web version of this article).

In some way, isoparametric element method involves two polynomials: one for the curved boundary and another for the solution approximation. Conversely, the method proposed in this work uses a unique polynomial for the two associated operations. Despite, the study in [27] presents some fundamental ingredients for the polynomial reconstructions under curved boundaries, the present paper proposes a simpler approach where all the integration procedures are performed on the polygonal domain.

This document is divided in seven sections. After the introduction, we formulate in Section 2 the problem we will consider and the mesh notations, while we present the polynomial reconstructions in Section 3. Section 4 is dedicated to the curved boundary where we detail the inclusion of the Dirichlet condition prescribed on the physical boundary. We present in Section 5 the very high-order finite volume and in Section 6 the numerical experiments. We end the document with the conclusions of this work and some perspectives.

2. Problem formulation and geometry

Let Ω be an open bounded domain of $\mathbb{R}^2$ with boundary $\partial\Omega$. We assume that the boundary is a regular Jordan curve which admits local parametrizations. We seek function $\phi \equiv \phi(x)$, $x \equiv (x_1, x_2)$, solution of the steady-state convection–diffusion equation

$$\nabla \cdot (u\phi - \kappa \nabla \phi) = f, \qquad \text{in } \Omega, \tag{1}$$

where $u = (u_1, u_2) \equiv (u_1(x), u_2(x))$ is a velocity field, $\kappa \equiv \kappa(x)$ is a diffusion coefficient, and $f \equiv f(x)$ is a regular source term in $\overline{\Omega}$, and where a Dirichlet condition is prescribed on the boundary $\partial\Omega$ with a given regular function $\phi_{\mathrm{D}} \equiv \phi_{\mathrm{D}}(x)$.

A mesh $\mathcal{M}$ is a set of I non-overlapping convex polygonal cells c_i, without gap, $i \in \mathcal{C}_{\mathcal{M}} = \{1, \ldots, I\}$, and we denote by

$$\Omega_\Delta = \bigcup_{i \in \mathcal{C}_{\mathcal{M}}} c_i$$

the computational domain and by $\partial\Omega_\Delta$ the computational boundary associated to the mesh $\mathcal{M}$. Ω_Δ should be a representative domain approximation of Ω and $\partial\Omega_\Delta$ is the associated approximation of $\partial\Omega$. To this end, we assume that the nodes on $\partial\Omega_\Delta$ also belong to $\partial\Omega$. We adopt the notations detailed hereafter (see Fig. 1):

- for any cell c_i we denote by ∂c_i its boundary and by $|c_i|$ its area; the reference cell point is denoted by m_i which can be any point in c_i (in the present work we consider the centroid);
- two different cells c_i and c_j share a common edge e_{ij} whose length is denoted by $|e_{ij}|$ and $n_{ij} = (n_{1,ij}, n_{2,ij})$ is the unit normal vector to e_{ij} outward to c_i, *i.e.* $n_{ij} = -n_{ji}$; the reference edge point is m_{ij} which can be any point on e_{ij} (in the present work we consider the midpoint); if an edge of c_i belongs to the boundary $\partial\Omega_\Delta$, the index j is replaced by letter D;
- for any edge e_{ij}, we denote by $q_{ij,r}$, $r = 1, \ldots, R$, the Gaussian integration points and ζ_r the associated weights;
- for any cell c_i we associate the index set of neighbor cells $\nu(i) \subset \{1, \cdots, I\} \cup \{\mathrm{D}\}$ such that $j \in \nu(i)$ if e_{ij} is a common edge between cells c_i and c_j or with the boundary $\partial\Omega_\Delta$ if $j = \mathrm{D}$.

We enhance that Ω is not a polygonal domain. So, the physical domain Ω and its polygonal approximation Ω_Δ do not coincide, and this usually leads to a significant accuracy degradation of the numerical approximation.

3. Polynomial reconstruction

The polynomial reconstruction is a powerful tool to provide an accurate local representation of the underlying solution, see [28,29] for unstructured grids and hyperbolic problems. In [30] a methodology was proposed in the context of convection–diffusion problems to achieve very high accurate approximations of the gradient fluxes and take into account

boundary conditions. The authors introduced different types of polynomial reconstructions namely the conservative reconstruction in cells and on boundary edges and the non-conservative reconstruction on inner edges, in order to compute approximations of the convective and the diffusive fluxes. In this work we mainly follows this methodology of reconstruction but applied in the specific but important case of curved boundaries.

3.1. Stencil and data

A stencil is a collection of cells situated in the vicinity of a reference geometrical entity, for instance an edge or a cell, where the number of elements of the stencil shall depend on the degree d of the polynomial function we intend to construct. So, for each edge e_{ij} and cell c_i we associate stencils S_{ij} and S_i, respectively, consisting of the indices of neighbor cells.

Remark 3.1. A polynomial reconstruction of degree d requires $n_d = (d+1)(d+2)/2$ coefficients in 2D. So, in practice, a stencil consists of the N_d closest cells to each geometrical entity (edge or cell) with $N_d \geq n_d$ (we consider $N_d \approx 1.5 n_d$ for the sake of robustness).

To compute the polynomial reconstructions we need the data associated to each cell of the stencil. To this end, we assume that vector $\Phi = (\phi_i)_{i\in\mathcal{C}_\mathcal{M}}$ gathers the approximation of the mean-value of ϕ over each cell, *i.e.*

$$\phi_i \approx \frac{1}{|c_i|}\int_{c_i} \phi \, \mathrm{d}x.$$

3.2. Conservative reconstruction for cells

For each cell c_i, the local d-th degree polynomial approximation of the underlying solution ϕ, based on vector Φ, is defined as

$$\phi_i(x) = \phi_i + \sum_{1\leq|\alpha|\leq d} \mathcal{R}_i^\alpha \left[(x-m_i)^\alpha - M_i^\alpha\right],$$

where $\alpha = (\alpha_1, \alpha_2)$ with $|\alpha| = \alpha_1 + \alpha_2$ and the convention $x^\alpha = x_1^{\alpha_1} x_2^{\alpha_2}$. Vector $\mathcal{R}_i = (\mathcal{R}_i^\alpha)_{1\leq|\alpha|\leq d}$ gathers the polynomial coefficients, and $M_i^\alpha = \frac{1}{|c_i|}\int_{c_i}(x-m_i)^\alpha \, \mathrm{d}x$ in order to guarantee the conservation property

$$\frac{1}{|c_i|}\int_{c_i} \phi_i(x) \, \mathrm{d}x = \phi_i.$$

For a given stencil S_i, we consider the quadratic functional

$$E_i(\mathcal{R}_i) = \sum_{q\in S_i}\left[\frac{1}{|c_q|}\int_{c_q}\phi_i(x)\,\mathrm{d}x - \phi_q\right]^2. \tag{2}$$

We denote by $\widehat{\mathcal{R}}_i$ the unique vector which minimizes the quadratic functional (2) and we set $\widehat{\phi}_i(x)$ the polynomial which corresponds to the best approximation in the least squares sense.

3.3. Non-conservative reconstruction for inner edges

For each inner edge e_{ij}, the local d-th degree polynomial approximation of the underlying solution ϕ, based on vector Φ, is defined as

$$\phi_{ij}(x) = \sum_{0\leq|\alpha|\leq d} \mathcal{R}_{ij}^\alpha (x-m_{ij})^\alpha,$$

where vector $\mathcal{R}_{ij} = (\mathcal{R}_{ij}^\alpha)_{0\leq|\alpha|\leq d}$ gathers the polynomial coefficients (notice that in this case $|\alpha|$ starts with 0). For a given stencil S_{ij} with $\#S_{ij}$ elements and vector $\omega_{ij} = (\omega_{ij,q})_{q=1,\ldots,\#S_{ij}}$ of positive weights of the reconstruction, we consider the quadratic functional

$$E_{ij}(\mathcal{R}_{ij}) = \sum_{q\in S_{ij}} \omega_{ij,q}\left[\frac{1}{|c_q|}\int_{c_q}\phi_{ij}(x)\,\mathrm{d}x - \phi_q\right]^2. \tag{3}$$

We denote by $\widetilde{\mathcal{R}}_{ij}$ the unique vector which minimizes the quadratic functional (3) and we set $\widetilde{\phi}_{ij}(x)$ the polynomial which corresponds to the best approximation in the least squares sense.

Remark 3.2. The weights are fundamental to provide the maximum principle and the stability of the scheme. In the simulations, we shall prescribe $\omega_{ij,q} = 3$ for the adjacent cells while we set $\omega_{ij,q} = 1$ for the other cells of the stencil. A deeper analysis to justifying the weights choice is given in [27,30].

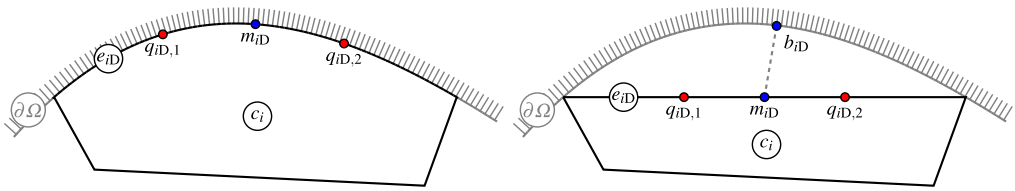

Fig. 2. The physical boundary $\partial\Omega$ and the boundary edge e_{iD} with Gauss points (red dots associated to a two-point quadrature rule) and edge midpoints m_{iD} (blue dots): left – situation when curved cells are considered; right – situation considered in this work with straight-edge cell and an associated collocation point b_{iD} associated to m_{iD}. (For interpretation of the references to color in this figure legend, the reader is referred to the web version of this article).

3.4. Conservative reconstruction for computational boundary edges

We treat the computational boundary edges in a particular way in order to take into account the prescribed Dirichlet condition. For each boundary edge e_{iD} on $\partial\Omega_\Delta$, the local d-th degree polynomial approximation of the underlying solution ϕ is defined as

$$\boldsymbol{\phi}_{iD}(x;\psi_{iD}) = \psi_{iD} + \sum_{1\le|\alpha|\le d} \mathcal{R}^{\alpha}_{iD}\left[(x-m_{iD})^{\alpha} - M^{\alpha}_{iD}\right],$$

where vector $\mathcal{R}_{iD} = (\mathcal{R}^{\alpha}_{iD})_{1\le|\alpha|\le d}$ gathers the polynomial coefficients, $\psi_{iD}\in\mathbb{R}$ is a free parameter which shall be set later, and $M^{\alpha}_{iD} = (p_{iD}-m_{iD})^{\alpha}$ in order to guarantee the conservation property

$$\psi_{iD} = \boldsymbol{\phi}_{iD}(p_{iD};\psi_{iD}), \tag{4}$$

with p_{iD} a given collocation point. The crucial point is that p_{iD} will be a distinct point from midpoint $m_{iD}\in e_{iD}$. For a given stencil S_{iD} with $\#S_{iD}$ elements and vector $\omega_{iD} = (\omega_{iD,q})_{q=1,\dots,\#S_{iD}}$ of positive weights of the reconstruction, we consider the quadratic functional

$$E_{iD}(\mathcal{R}_{iD}) = \sum_{q\in S_{iD}} \omega_{iD,q}\left[\frac{1}{|c_q|}\int_{c_q}\boldsymbol{\phi}_{iD}(x;\psi_{iD})\,\mathrm{d}x - \phi_q\right]^2. \tag{5}$$

We denote by $\widehat{\mathcal{R}}_{iD}$ the unique vector which minimizes the quadratic functional (5) and we set $\widehat{\boldsymbol{\phi}}_{iD}(x;\psi_{iD})$ the polynomial which corresponds to the best approximation in the least squares sense for the given parameter ψ_{iD} and point p_{iD}.

Remark 3.3. The motivation for introducing the weights either for the case of a non-conservative polynomial reconstruction or for a conservative polynomial reconstruction for computational boundary edges is presented in [30] as well as the importance to set larger values for the adjacent cells. We refer the reader to [30] for more details.

4. Reconstructions for Off-site Data (ROD)

4.1. The Ollivier-Gooch and Van Altena method

An accurate approximation of boundary conditions on curved boundaries is of paramount importance when dealing with very high-order methods, since to approximate a curved boundary with a polygonal mesh generally leads to a second-order approximation [3]. The seminal paper of Ollivier-Gooch and Van Altena [23] introduces a technique for constraining the least-squares problem associated to the polynomial reconstructions on the boundary elements. Such approach requires that the reconstructed solution satisfies the boundary condition exactly at the flux integration points (collocation points) [25]. In order to properly represent the boundary condition, the mesh has to fit with the physical boundary, that is, the edges of the mesh are curved for matching the real boundary (see Fig. 2). As mentioned in the introduction, this approach brings several drawbacks: one has to carefully design Gauss quadrature procedures to take into account curved boundaries for preserving the accuracy [26], and designing boundary-fitted mesh for non polygonal domains is still nowadays a difficult task [3]. In this work we avoid the difficult construction of boundary-fitted mesh and solely work on the easy to construct polygonal mesh.

4.2. The ROD method

We propose a different technique to prescribe Dirichlet conditions on curved boundaries. The main idea is to distinguish the computational domain from the physical one, and, perform all computations on the polygonal cells, but taking into account the information located on the physical boundary via the polynomial reconstructions. “Off-site Data” method is

meant to remind that the scheme and the solutions are acting on the computational domain Ω_Δ, but including information which is not associated to any geometrical entity of Ω_Δ (cell, edge, or point). The main advantages are:

- numerical integration of flux or functions are only carried out on the polygonal domain and not on the complex physical domain;
- no curved elements are required, only the computational polygonal mesh is necessary;
- no geometrical transformations are required involving possibly complex Jacobian functions for the integrals;
- no Gaussian points on the physical boundary $\partial\Omega$ are required;
- the method design does not depend on the number of spacial dimensions.

The technique is intrinsically associated to the conservative polynomial reconstruction given in Section 3.4 where, for a given edge $e_{i\mathrm{D}}$ of the computational boundary $\partial\Omega_\Delta$, we define the polynomial approximation $\widehat{\boldsymbol{\phi}}_{i\mathrm{D}}(x;\psi_{i\mathrm{D}})$ depending on parameter $\psi_{i\mathrm{D}}$ and point $p_{i\mathrm{D}}$ which satisfies the conservation property (4). We also mention that $b_{i\mathrm{D}}$ stands for a point on the physical boundary $\partial\Omega$, somewhere facing edge $e_{i\mathrm{D}}$ as depicted in Fig. 2-right while $m_{i\mathrm{D}}$ stands for the edge midpoint.

The Dirichlet condition will be enforced via a clever choice of the values of free parameter $\psi_{i\mathrm{D}}$ and point $p_{i\mathrm{D}}$. As a consequence one has to design a procedure to compute the free parameter such that we simultaneously satisfy the conservation and provide a very high-order approximation of the boundary condition.

4.2.1. Second-order approximation

A simple approach consists in using $p_{i\mathrm{D}} = m_{i\mathrm{D}}$ and in setting the free parameter as $\psi_{i\mathrm{D}} = \phi_{\mathrm{D}}(m_{i\mathrm{D}})$. Such a choice provides no more than a second-order convergence rate since $m_{i\mathrm{D}}$ does not represent exactly the physical boundary. Moreover, we need an extension of function ϕ_{D} in the neighborhood of the boundary to guarantee that $\phi_{\mathrm{D}}(m_{i\mathrm{D}})$ makes sense since $m_{i\mathrm{D}} \notin \partial\Omega$.

4.2.2. Very high-order approximation: ROD1

In order to enforce the Dirichlet condition more accurately, we now set $p_{i\mathrm{D}} = b_{i\mathrm{D}}$ and the free parameter $\psi_{i\mathrm{D}} = \phi_{\mathrm{D}}(b_{i\mathrm{D}})$. Notice that the flux integration will nonetheless be computed on the straight edge of the computational mesh as presented in Section 5.2 and not on the physical boundary as in [23]. We expect a very high-order accuracy since the reconstruction satisfies the Dirichlet condition at one point associated to the true physical boundary.

4.2.3. Very high-order approximation: ROD2

The major drawback of the method ROD1 is that the least-squares problem (5) is based on point $p_{i\mathrm{D}}$ that depends on the physical domain boundary and if the physical boundary evolves, for instance for time dependent moving domains or interface tracking problems, one has to rebuild the whole reconstruction procedure for boundary cells/edges. We improve the previous technique by decoupling the Dirichlet condition from the interpolation problem still preserving the very high-order accuracy. We start again by setting the collocation point $p_{i\mathrm{D}} = m_{i\mathrm{D}}$ as in the second-order method. Hence the least-squares procedure (5) no longer depends on the physical boundary position. Next the free parameter $\psi_{i\mathrm{D}}$ is computed in a special way. To this end, let us introduce the functional

$$\psi_{i\mathrm{D}} \to \mathcal{B}_{i\mathrm{D}}(b_{i\mathrm{D}};\psi_{i\mathrm{D}}) = \widehat{\boldsymbol{\phi}}_{i\mathrm{D}}(b_{i\mathrm{D}};\psi_{i\mathrm{D}}) - \phi_{\mathrm{D}}(b_{i\mathrm{D}}). \tag{6}$$

Notice that $\mathcal{B}_{i\mathrm{D}}$ is affine with respect to $\psi_{i\mathrm{D}}$.

We now seek for $\psi^*_{i\mathrm{D}}$ as the unique solution which satisfies the affine problem

$$\mathcal{B}_{i\mathrm{D}}(b_{i\mathrm{D}};\psi_{i\mathrm{D}}) = 0. \tag{7}$$

We compute the solution of this problem by taking two values $\psi^1_{i\mathrm{D}}, \psi^2_{i\mathrm{D}} \in \mathbb{R}$, $\psi^1_{i\mathrm{D}} \neq \psi^2_{i\mathrm{D}}$, and after some algebraic simplifications one get

$$\psi^*_{i\mathrm{D}} = \frac{\psi^2_{i\mathrm{D}}\mathcal{B}_{i\mathrm{D}}(b_{i\mathrm{D}};\psi^1_{i\mathrm{D}}) - \psi^1_{i\mathrm{D}}\mathcal{B}_{i\mathrm{D}}(b_{i\mathrm{D}};\psi^2_{i\mathrm{D}})}{\mathcal{B}_{i\mathrm{D}}(b_{i\mathrm{D}};\psi^1_{i\mathrm{D}}) - \mathcal{B}_{i\mathrm{D}}(b_{i\mathrm{D}};\psi^2_{i\mathrm{D}})}. \tag{8}$$

In other words, we adjust the free parameter at point $m_{i\mathrm{D}}$ to satisfy the Dirichlet condition at $b_{i\mathrm{D}}$. In practice, we take $\psi^1_{i\mathrm{D}} = \phi_{\mathrm{D}}(m_{i\mathrm{D}})$ and $\psi^2_{i\mathrm{D}} = \phi_{\mathrm{D}}(m_{i\mathrm{D}}) + 1$ since $\psi^*_{i\mathrm{D}}$ is supposed to be close to $\phi_{\mathrm{D}}(m_{i\mathrm{D}})$.

Remark 4.1. The methods ROD1 and ROD2 mainly differ in the structure of the matrix that compute the polynomial coefficients with respect to the data and the Dirichlet condition. In the first case, the matrix depends on the position of the point where the Dirichlet is evaluated but does not require the additional treatment given in relation (8). On the contrary, the ROD2 method provides a matrix that does not depend of the position of the Dirichlet condition but an extra-computational effort is necessary to fix the free parameter with (8). To sum-up, if one considers a fix curved domain, the ROD1 method is more efficient whereas the ROD2 technique is well-adapted to situations where the physical boundary changes with time or during an iterative process.

Remark 4.2. The coefficients $\widehat{\mathcal{R}}_{i\mathrm{D}}$ of the polynomial function $\widehat{\boldsymbol{\phi}}_{i\mathrm{D}}(x;\psi_{i\mathrm{D}})$ are obtained as the matrix-vector product between the Moore-Penrose matrix associated to the least-square problem and the vector of cell values in the stencil [30]. The matrix structure does not depend on the physical boundary position by construction but only depends on the computational mesh. The Dirichlet condition is only prescribed via functional (6) and satisfies condition (7).

5. Very high-order finite volume scheme

5.1. Generic finite volume scheme

To obtain a finite volume scheme, Eq. (1) is integrated over each cell c_i and applying the divergence theorem we get

$$\int_{\partial c_i} (u\phi - \kappa \nabla \phi) \cdot n_i \mathrm{d}s = \int_{c_i} f \mathrm{d}x,$$

where ∂c_i is the cell boundary and n_i is the associated outward unit vector. Considering the Gaussian quadrature with $R \in \mathbb{N}^*$ points for the line integrals, *i.e.* of order $2R$, we get the residual expression

$$\sum_{j \in \nu(i)} |e_{ij}| \left[\sum_{r=1}^{R} \zeta_r \left(\mathbb{F}^{\mathrm{C}}_{ij,r} + \mathbb{F}^{\mathrm{D}}_{ij,r} \right) \right] - f_i |c_i| = \mathcal{O}(h_i^{2R}), \tag{9}$$

with the physical fluxes given by

$$\mathbb{F}^{\mathrm{C}}_{ij,r} = u(q_{ij,r}) \cdot n_{ij} \phi(q_{ij,r}) \qquad \text{and} \qquad \mathbb{F}^{\mathrm{D}}_{ij,r} = -\kappa(q_{ij,r}) \nabla \phi(q_{ij,r}) \cdot n_{ij},$$

and with $h_i = \max_{j \in \nu(i)} |e_{ij}|$, while f_i stands for an approximation of order $2R$ of the mean value of f over cell c_i. Notice that if cell c_i is not triangular, we split it into sub-triangles which share the cell centroid as a common vertex and apply the quadrature rule on each sub-triangle as in [31]. Using the different polynomial reconstructions see previous sections, we design the numerical scheme with two main ingredients: the flux computation and the solver. We use a similar technique proposed in [27,30], particularly the matrix-free approach is adopted, based on the residual operator construction.

5.2. Numerical fluxes

Numerical fluxes are computed with respect to the edges:

- for the inner edges e_{ij}, the fluxes at the quadrature point $q_{ij,r}$ write

$$\mathcal{F}^{\mathrm{C}}_{ij,r} = \left[u(q_{ij,r}) \cdot n_{ij} \right]^{+} \widehat{\boldsymbol{\phi}}_i(q_{ij,r}) + \left[u(q_{ij,r}) \cdot n_{ij} \right]^{-} \widehat{\boldsymbol{\phi}}_j(q_{ij,r}),$$
$$\mathcal{F}^{\mathrm{D}}_{ij,r} = -\kappa(q_{ij,r}) \nabla \widetilde{\boldsymbol{\phi}}_{ij}(q_{ij,r}) \cdot n_{ij};$$

- for the boundary edges $e_{i\mathrm{D}}$, the fluxes at the quadrature point $q_{i\mathrm{D},r}$ write

$$\mathcal{F}^{\mathrm{C}}_{i\mathrm{D},r} = [u(q_{i\mathrm{D},r}) \cdot n_{i\mathrm{D}}]^{+} \widehat{\boldsymbol{\phi}}_i(q_{i\mathrm{D},r}) + [u(q_{i\mathrm{D},r}) \cdot n_{i\mathrm{D}}]^{-} \widehat{\boldsymbol{\phi}}_{i\mathrm{D}}(q_{i\mathrm{D},r}),$$
$$\mathcal{F}^{\mathrm{D}}_{i\mathrm{D},r} = -\kappa(q_{i\mathrm{D},r}) \nabla \widehat{\boldsymbol{\phi}}_{i\mathrm{D}}(q_{i\mathrm{D},r}) \cdot n_{i\mathrm{D}}.$$

Notice that all the fluxes are computed on the edges of the computational domain without any reference to the physical domain. The Dirichlet condition on $\partial\Omega$ is implicitly contained in the polynomial reconstructed function $\widehat{\boldsymbol{\phi}}_{i\mathrm{D}}$.

5.3. Residual operator and solver

For any vector Φ in $\mathbb{R}^I$, we define the residual operators for cells c_i, $i = 1, \ldots, I$, as

$$\mathcal{G}_i(\Phi) = \sum_{j \in \nu(i)} |e_{ij}| \left[\sum_{r=1}^{R} \zeta_r \left(\mathcal{F}^{\mathrm{C}}_{ij,r} + \mathcal{F}^{\mathrm{D}}_{ij,r} \right) \right] - f_i |c_i|,$$

which corresponds to the finite volume scheme (9) cast in residual form. Gathering all the components of the residuals provides a global affine operator $\mathcal{G}(\Phi) = (\mathcal{G}_i(\Phi))_{i \in \mathcal{C}_\mathcal{M}}$ and we seek vector $\Phi^\star \in \mathbb{R}^I$, solution of the problem $\mathcal{G}(\Phi) = 0$. The GMRES method, powered by a preconditioning matrix, is carried out to compute an approximation of $\Phi^\star$ as in [27,30].

6. Numerical results

In order to validate the implementation of the methods and assess the accuracy and the convergence rates, we manufacture several analytic solutions on specific domains which require the computation of an associated source term to satisfy Eq. (1). Vector $\Phi^\star = (\phi_i^\star)_{i \in \mathcal{C}_\mathcal{M}}$ gathers the numerical approximations of the mean values of ϕ while vector $\overline{\Phi} = (\overline{\phi}_i)_{i \in \mathcal{C}_\mathcal{M}}$ gathers the exact mean values $\overline{\phi}_i$ of ϕ, that is $\overline{\phi}_i = (1/|c_i|) \int_{c_i} \phi \, \mathrm{d}x$.

The normalized L^1- and L^∞-norm errors, denoted by E_1 and E_∞, are computed, respectively, as

$$E_1(\mathcal{M}) = \frac{\sum_{i \in \mathcal{C}_\mathcal{M}} |\phi_i^\star - \overline{\phi}_i| |c_i|}{\sum_{i \in \mathcal{C}_\mathcal{M}} |\overline{\phi}_i| |c_i|} \qquad \text{and} \quad E_\infty(\mathcal{M}) = \frac{\max_{i \in \mathcal{C}_\mathcal{M}} |\phi_i^\star - \overline{\phi}_i|}{\sum_{i \in \mathcal{C}_\mathcal{M}} |\overline{\phi}_i| |c_i|}.$$

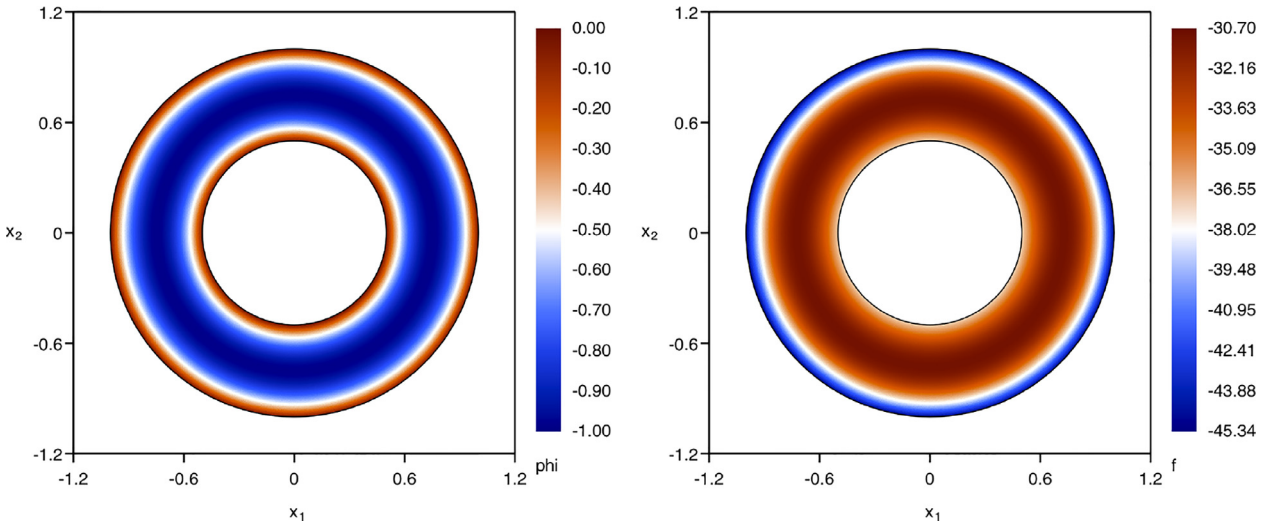

Fig. 3. Manufactured solution (left panel) and source term (right panel) for the low Péclet number test case. (For interpretation of the colormap in this figure, the reader is referred to the web version of this article).

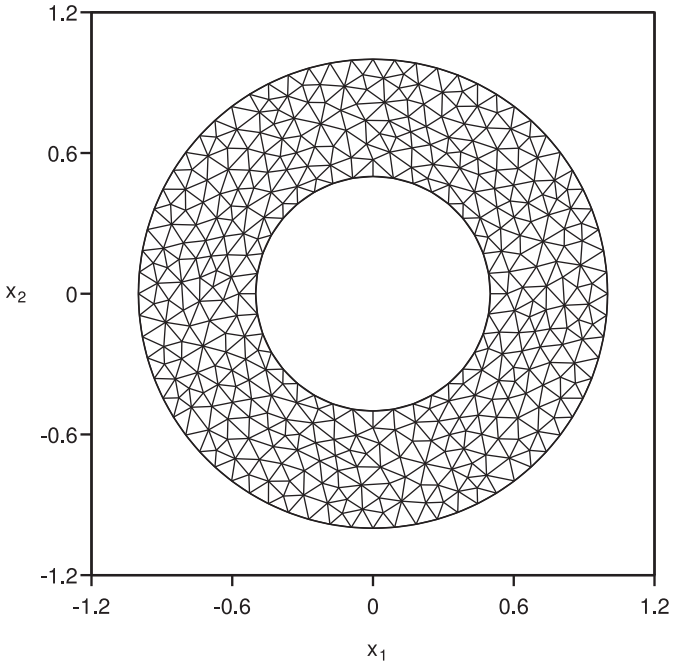

Fig. 4. Coarse uniform triangular Delaunay mesh prescribed for the annulus domain.

The convergence rate for the normalized L^1- and L^∞-norm errors between two different meshes $\mathcal{M}_1$ and $\mathcal{M}_2$, with DOF_1 and DOF_2 degrees of freedom, respectively, where $DOF_1 \neq DOF_2$, is evaluated as

$$O_\alpha(\mathcal{M}_1, \mathcal{M}_2) = 2\frac{|\log(E_\alpha(\mathcal{M}_1)/E_\alpha(\mathcal{M}_2))|}{|\log(DOF_1/DOF_2)|}, \qquad \alpha \in \{1, \infty\}.$$

In all the simulations, the weights in functionals (3) and (5) are set to $\omega_{ij,q} = 3$, $i \in \mathcal{C}_\mathcal{M}$, $j \in \nu(i)$, $q \in S_{ij}$, if e_{ij} is an edge of c_q and $\omega_{ij,q} = 1$, otherwise.

For the sake of simplicity, we name the method given in Section 4.2.1 as "second-order method", the one given in Section 4.2.2 as "ROD1 method", and the proposed method, presented in Section 4.2.3, as "ROD2 method". The methodology of validation consists in observing the rates of convergence under mesh refinement when very high-order polynomial reconstructions ($\mathbb{P}_k$, $k = 1, 3, 5$) are employed for different strategies dealing with Dirichlet boundary conditions defined on

Table 1
Annulus problem for low Péclet number – Errors and convergence rates for the second-order, ROD1, and ROD2 methods with uniform triangular Delaunay meshes.

Second-order method (Section 4.2.1)												
	$\mathbb{P}_1$				$\mathbb{P}_3$				$\mathbb{P}_5$			
DOF	E_1	O_1	E_∞	O_∞	E_1	O_1	E_∞	O_∞	E_1	O_1	E_∞	O_∞
736	2.17E−02	–	4.56E−02	–	3.87E−03	–	9.88E−03	–	3.84E−03	–	9.82E−03	–
2828	6.62E−03	1.77	1.24E−02	1.94	1.04E−03	1.95	2.79E−03	1.88	1.04E−03	1.94	2.81E−03	1.86
11,500	1.52E−03	2.10	3.59E−03	1.76	2.63E−04	1.97	7.11E−04	1.95	2.63E−04	1.97	7.12E−04	1.96
45,248	4.07E−04	1.93	1.01E−03	1.84	6.74E−05	1.99	1.85E−04	1.97	6.74E−05	1.99	1.85E−04	1.97
177,880	1.35E−04	1.61	3.08E−04	1.74	1.71E−05	2.01	4.71E−05	2.00	1.71E−05	2.01	4.71E−05	2.00
Reconstruction for Off-site Data (ROD1) method (Section 4.2.2)												
	$\mathbb{P}_1$				$\mathbb{P}_3$				$\mathbb{P}_5$			
DOF	E_1	O_1	E_∞	O_∞	E_1	O_1	E_∞	O_∞	E_1	O_1	E_∞	O_∞
736	2.06E−02	–	4.55E−02	–	1.55E−04	–	9.14E−04	–	5.06E−05	–	2.22E−04	–
2828	6.21E−03	1.78	1.21E−02	1.97	9.63E−06	4.13	6.51E−05	3.93	3.30E−07	7.48	4.95E−06	5.65
11,500	1.43E−03	2.10	3.49E−03	1.77	4.92E−07	4.24	3.93E−06	4.00	5.43E−09	5.85	9.15E−08	5.69
45,248	3.82E−04	1.93	1.02E−03	1.80	3.72E−08	3.77	4.13E−07	3.29	9.38E−11	5.93	2.84E−09	5.07
177,880	1.28E−04	1.59	3.27E−04	1.66	3.76E−09	3.35	2.44E−08	4.14	1.76E−12	5.81	4.21E−11	6.15
Reconstruction for Off-site Data (ROD2) method (Section 4.2.3)												
	$\mathbb{P}_1$				$\mathbb{P}_3$				$\mathbb{P}_5$			
DOF	E_1	O_1	E_∞	O_∞	E_1	O_1	E_∞	O_∞	E_1	O_1	E_∞	O_∞
736	2.07E−02	–	4.56E−02	–	1.54E−04	–	9.01E−04	–	4.74E−05	–	2.13E−04	–
2828	6.22E−03	1.78	1.21E−02	1.97	9.67E−06	4.11	6.47E−05	3.91	3.25E−07	7.40	4.91E−06	5.60
11,500	1.43E−03	2.10	3.50E−03	1.77	4.92E−07	4.25	3.92E−06	4.00	5.39E−09	5.84	9.17E−08	5.68
45,248	3.82E−04	1.93	1.02E−03	1.80	3.71E−08	3.77	4.13E−07	3.29	9.43E−11	5.91	2.84E−09	5.07
177,880	1.28E−04	1.59	3.27E−04	1.66	3.76E−09	3.35	2.44E−08	4.13	1.76E−12	5.82	4.21E−11	6.15

the physical curved domains. Only smooth solutions of the steady-state two-dimensional convection–diffusion equation are considered. The different curved physical domains are

- An annulus domain in Section 6.1. We simulate with triangular (possibly refined) grids low Péclet number, high Péclet number and pure convection problems.
- A rose-shaped domain in Section 6.2. A deformation of the annulus allows to define branches on the interior and exterior boundaries. We simulate with triangular and quadrilateral grids two different cases, a rose with three-three branches and another five-three branches.

6.1. Annulus domain

In this first set of numerical tests we consider an annulus domain with center at (0, 0) characterized by the interior and exterior circumferences Γ_I and Γ_E, respectively, with radius $r_I = 0.5$ and $r_E = 1$. For the convection–diffusion problem (1), we prescribe a constant radial velocity u and $\kappa = 1$. We then seek for a manufactured solution, invariant by rotation, given be

$$\phi(x_1, x_2) = a\big(\exp(ur') + \exp(-ur') + b\big), \qquad r' \equiv r'(r) = \frac{(2r - (r_E + r_I))}{(r_E - r_I)},$$

with $r^2 = x_1^2 + x_2^2$ such that $r' \in [-1, 1]$. We also prescribe homogeneous Dirichlet conditions on the two boundaries Γ_I and Γ_E and deduce that $b = -\exp(u) - \exp(-u)$ while $a = 1/(\exp(u) + \exp(-u) - 2)$ guarantees the property $\phi \in [-1, 0]$ in Ω. The associated source term f is obtained after substituting the solution into Eq. (1).

Low Péclet number. We first address the low Péclet number situation setting $u = 1$. We plot in Fig. 3 the manufactured solution and the source term. The simulations were carried out with successive refined uniform triangular Delaunay meshes (see Fig. 4). Observe that boundary vertices belong to the true physical domain boundary.

We report in Table 1 the errors and the convergence rates for the second-order, and the two ROD methods. The second-order approach provides at most a second-order convergence for both error norms, whatever the degree of the polynomial reconstruction. These results are expected since the Dirichlet condition is affected with a mismatch of order $\mathcal{O}(h^2)$ due to the erroneous location with respect to the physical boundary. The two other methods recover the optimal order and achieve an effective second-, fourth-, and sixth-order convergence rates for $\mathbb{P}_1$, $\mathbb{P}_3$, and $\mathbb{P}_5$ polynomial reconstructions, respectively, while no oscillations are reported. The accuracy of both methods are quite comparable and clearly overcome the second-order limitation expected when dealing with the curved boundary with non-fitted cells.

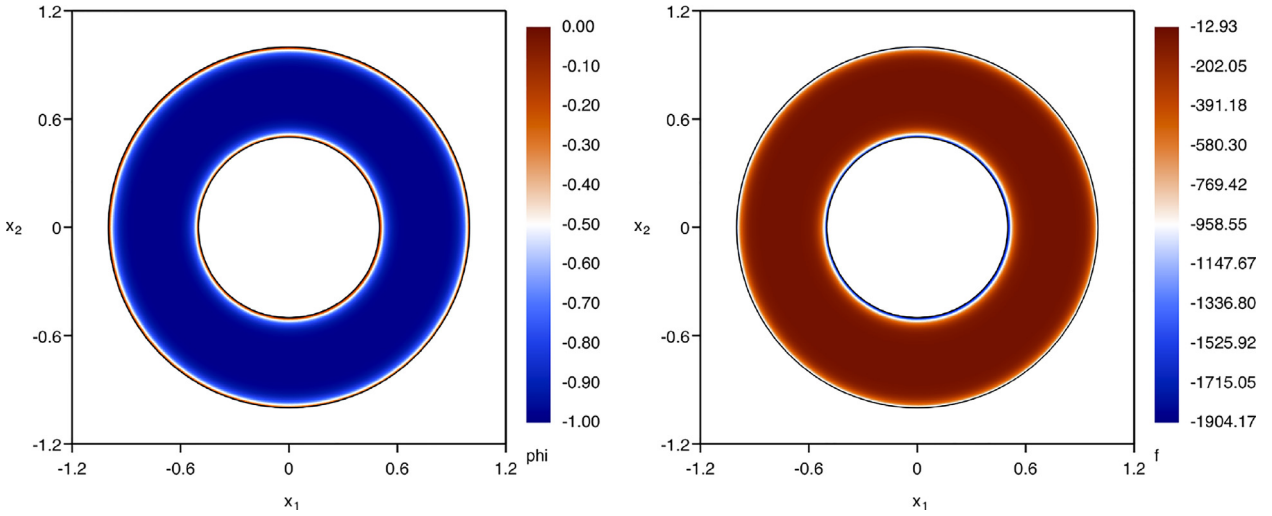

Fig. 5. Manufactured solution (left panel) and source term (right panel) for the high Péclet number test case. (For interpretation of the colormap in this figure, the reader is referred to the web version of this article).

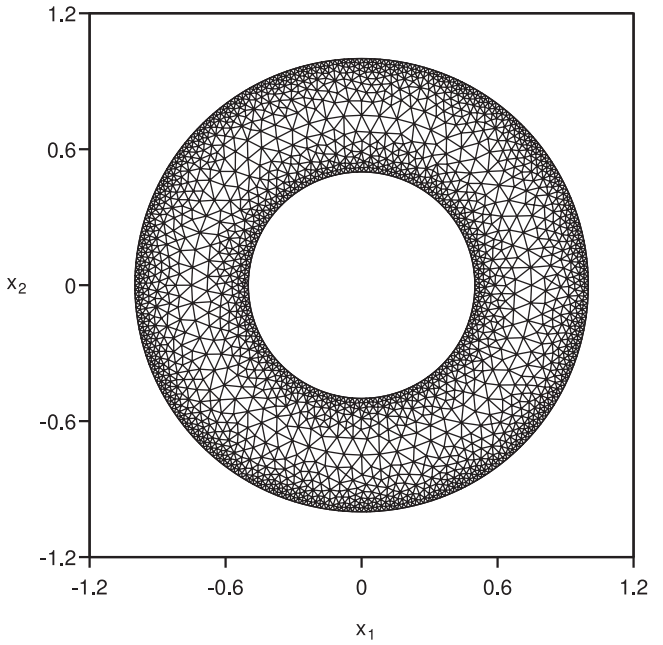

Fig. 6. Coarse non-uniform triangular Delaunay mesh prescribed for the annulus domain for the high Péclet number test case.

High Péclet number. Large Péclet number is prescribed taking $u = 10$ and we plot in Fig. 5 the manufactured solution and the source term. This test addresses the scheme robustness and accuracy to preserve the boundary condition when dealing with small boundary layers with respect to the dimension of the whole geometry. The simulations were carried out with successive refined Delaunay meshes plotted in Fig. 6 where, again, the boundary vertices belong to the physical boundary.The meshes are refined close to the boundaries to better capture the boundary layers.

In Table 2, we report the errors and the convergence rates for the three methods. As for the low Péclet problem the second-order method reaches at most a second-order convergence for both error norms while the two ROD methods achieve an effective second-, fourth-, and sixth-order convergence rates for $\mathbb{P}_1$, $\mathbb{P}_3$, and $\mathbb{P}_5$ polynomial reconstructions, respectively. We conclude that the very high-order methods effectively handle large Péclet number situations achieving optimal convergence rates without any oscillation.

Table 2
Annulus problem for high Péclet number — Errors and convergence rates for the second-order, ROD1, and ROD2 methods with adapted triangular Delaunay meshes.

Second-order method (Section 4.2.1)

	$\mathbb{P}_1$				$\mathbb{P}_3$				$\mathbb{P}_5$			
DOF	E_1	O_1	E_∞	O_∞	E_1	O_1	E_∞	O_∞	E_1	O_1	E_∞	O_∞
4292	1.16E−02	–	3.63E−02	–	6.36E−04	–	4.04E−03	–	1.20E−03	–	2.07E−03	–
16,398	2.73E−03	2.16	1.32E−02	1.51	2.11E−04	1.64	6.15E−04	2.81	2.48E−04	2.36	4.67E−04	2.22
63,364	3.57E−04	3.01	4.30E−03	1.66	5.74E−05	1.93	1.28E−04	2.32	6.10E−05	2.08	1.16E−04	2.06
250,732	1.17E−04	1.62	1.20E−03	1.86	1.53E−05	1.93	3.00E−05	2.11	1.53E−05	2.01	2.93E−05	2.01
996,002	8.10E−05	0.53	3.07E−04	1.98	3.85E−06	2.00	7.38E−06	2.03	3.85E−06	2.01	7.35E−06	2.00

Reconstruction for Off-site Data (ROD2) method (Section 4.2.2)

	$\mathbb{P}_1$				$\mathbb{P}_3$				$\mathbb{P}_5$			
DOF	E_1	O_1	E_∞	O_∞	E_1	O_1	E_∞	O_∞	E_1	O_1	E_∞	O_∞
4292	1.08E−02	–	3.46E−02	–	9.47E−04	–	2.43E−03	–	2.93E−04	–	5.83E−04	–
16,398	2.52E−03	2.17	1.27E−02	1.49	5.61E−05	4.22	2.14E−04	3.63	5.88E−06	5.83	1.48E−05	5.48
63,364	3.17E−04	3.07	4.19E−03	1.65	4.92E−06	3.60	1.68E−05	3.77	8.08E−08	6.34	2.69E−07	5.93
250,732	1.25E−04	1.35	1.17E−03	1.85	1.23E−07	5.36	1.42E−06	3.60	1.10E−09	6.24	5.65E−09	5.62
996,002	8.39E−05	0.58	3.01E−04	1.97	7.15E−09	4.13	8.87E−08	4.02	1.00E−11	6.82	8.52E−11	6.08

Reconstruction for Off-site Data (ROD2) method (Section 4.2.3)

	$\mathbb{P}_1$				$\mathbb{P}_3$				$\mathbb{P}_5$			
DOF	E_1	O_1	E_∞	O_∞	E_1	O_1	E_∞	O_∞	E_1	O_1	E_∞	O_∞
	$\mathbb{P}_1$				$\mathbb{P}_3$				$\mathbb{P}_5$			
DOF	E_1	O_1	E_∞	O_∞	E_1	O_1	E_∞	O_∞	E_1	O_1	E_∞	O_∞
4292	1.08E−02	–	3.46E−02	–	9.47E−04	–	2.43E−03	–	2.92E−04	–	5.83E−04	–
16,398	2.52E−03	2.17	1.27E−02	1.49	5.61E−05	4.22	2.14E−04	3.63	5.88E−06	5.83	1.48E−05	5.48
63,364	3.17E−04	3.07	4.19E−03	1.65	4.92E−06	3.60	1.68E−05	3.77	8.08E−08	6.34	2.69E−07	5.93
250,732	1.25E−04	1.35	1.17E−03	1.85	1.23E−07	5.36	1.42E−06	3.60	1.10E−09	6.24	5.65E−09	5.62
996,002	8.39E−05	0.58	3.01E−04	1.97	7.15E−09	4.13	8.87E−08	4.02	1.00E−11	6.82	8.52E−11	6.08

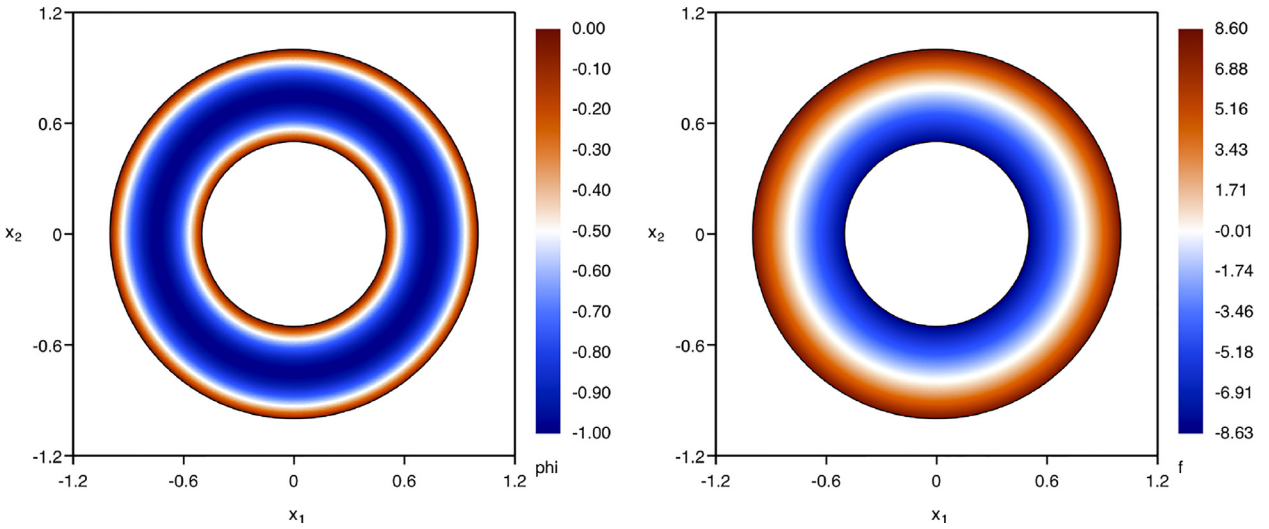

Fig. 7. Manufactured solution (left panel) and source term (right panel) for the pure convection test case. (For interpretation of the colormap in this figure, the reader is referred to the web version of this article).

Pure convection. We address the pure convection situation setting $\kappa = 0$ and $u = 1$ and plot in Fig. 7 the manufactured solution and the source term. The simulations were carried out with successive refined uniform triangular Delaunay meshes presented in Fig. 4 and, as in the previous tests, the boundary vertices belong to the boundary curves.

We report in Table 3, the errors and the convergence rates for the three methods. As in the previous situations, the second-order boundary approach is doomed to a second-order of accuracy while the two other methods efficiently handle the convection problem with curved boundaries with no oscillations and no artificial diffusion.

Table 3
Annulus problem for pure convection – Errors and convergence rates for the second-order, ROD1, and ROD2 methods with uniform triangular Delaunay meshes.

Second-order method (Section 4.2.1)

	$\mathbb{P}_1$				$\mathbb{P}_3$				$\mathbb{P}_5$			
DOF	E_1	O_1	E_∞	O_∞	E_1	O_1	E_∞	O_∞	E_1	O_1	E_∞	O_∞
736	1.01E−02	–	4.43E−02	–	6.78E−03	–	1.07E−02	–	6.88E−03	–	1.01E−02	–
2828	3.62E−03	1.52	2.35E−02	0.94	1.92E−03	1.88	2.92E−03	1.93	1.93E−03	1.89	2.85E−03	1.88
11,500	8.67E−04	2.04	1.07E−02	1.12	4.81E−04	1.97	7.19E−04	2.00	4.82E−04	1.98	7.18E−04	1.97
45,248	2.23E−04	1.98	1.91E−03	2.51	1.24E−04	1.98	1.86E−04	1.98	1.24E−04	1.98	1.86E−04	1.98
177,880	6.85E−05	1.72	4.07E−03	1.11	3.15E−05	2.00	4.72E−05	2.00	3.15E−05	2.00	4.72E−05	2.00

Reconstruction for Off-site Data (ROD1) method (Section 4.2.2)

	$\mathbb{P}_1$				$\mathbb{P}_3$				$\mathbb{P}_5$			
DOF	E_1	O_1	E_∞	O_∞	E_1	O_1	E_∞	O_∞	E_1	O_1	E_∞	O_∞
736	8.75E−03	–	3.87E−02	–	2.35E−04	–	1.26E−03	–	3.48E−05	–	1.32E−04	–
2828	3.45E−03	1.38	2.15E−02	0.87	2.47E−05	3.35	1.09E−04	3.63	1.25E−06	4.95	5.26E−06	4.79
11,500	8.07E−04	2.07	1.03E−02	1.05	1.58E−06	3.91	9.50E−06	3.48	2.34E−08	5.67	1.14E−07	5.46
45,248	2.06E−04	2.00	1.81E−03	2.54	1.21E−07	3.76	8.04E−07	3.61	5.04E−10	5.60	3.11E−09	5.26
177,880	6.49E−05	1.69	4.05E−03	1.17	8.45E−09	3.89	9.60E−08	3.10	8.65E−12	5.94	5.76E−11	5.83

Reconstruction for Off-site Data (ROD2) method (Section 4.2.3)

	$\mathbb{P}_1$				$\mathbb{P}_3$				$\mathbb{P}_5$			
DOF	E_1	O_1	E_∞	O_∞	E_1	O_1	E_∞	O_∞	E_1	O_1	E_∞	O_∞
736	8.75E−03	–	3.87E−02	–	2.36E−04	–	1.26E−03	–	3.57E−05	–	1.33E−04	–
2828	3.45E−03	1.38	2.15E−02	0.87	2.47E−05	3.35	1.10E−04	3.63	1.25E−06	4.98	5.27E−06	4.80
11,500	8.07E−04	2.07	1.03E−02	1.05	1.59E−06	3.91	9.50E−06	3.49	2.34E−08	5.68	1.14E−07	5.47
45,248	2.06E−04	2.00	1.81E−03	2.54	1.21E−07	3.76	8.04E−07	3.61	5.04E−10	5.60	3.11E−09	5.26
177,880	6.49E−05	1.69	4.05E−03	1.17	8.45E−09	3.89	9.61E−08	3.10	8.64E−12	5.94	5.76E−11	5.83

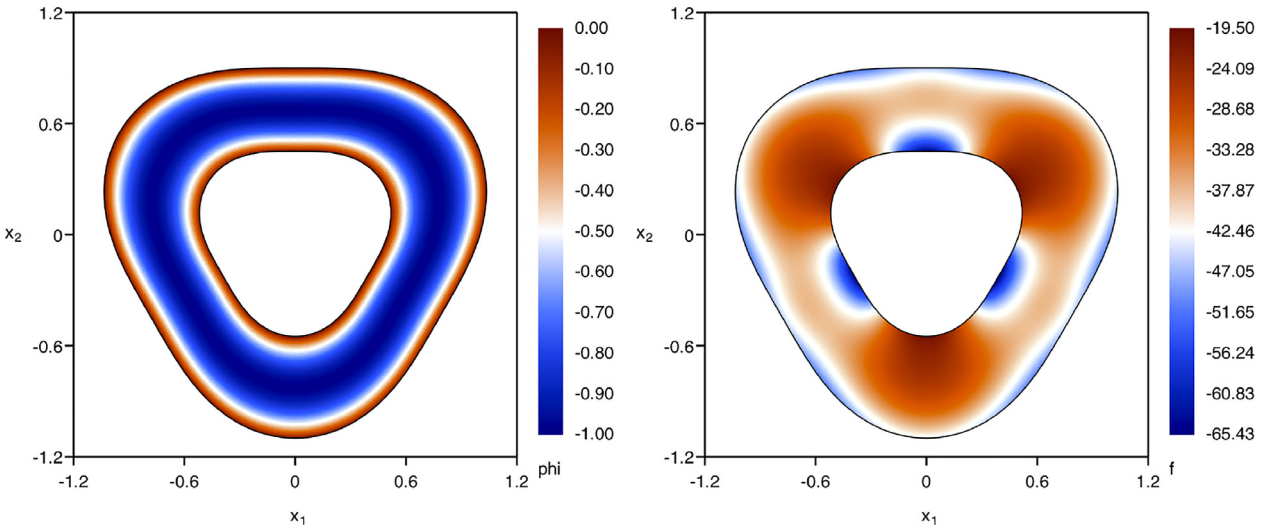

Fig. 8. Manufactured solution (left panel) and source term (right panel). (For interpretation of the colormap in this figure, the reader is referred to the web version of this article).

6.2. Rose-shaped domain

We now consider a more complex geometry where the annulus is transformed by a diffeomorphism mapping which consists in a periodic transformation of the boundaries in the following way:

$$\Gamma_I : \begin{bmatrix} x_1 \\ x_2 \end{bmatrix} = R_I(\theta;\alpha_I)\begin{bmatrix} \cos(\theta) \\ \sin(\theta) \end{bmatrix} \quad \text{and} \quad \Gamma_E : \begin{bmatrix} x_1 \\ x_2 \end{bmatrix} = R_E(\theta;\alpha_E)\begin{bmatrix} \cos(\theta) \\ \sin(\theta) \end{bmatrix},$$

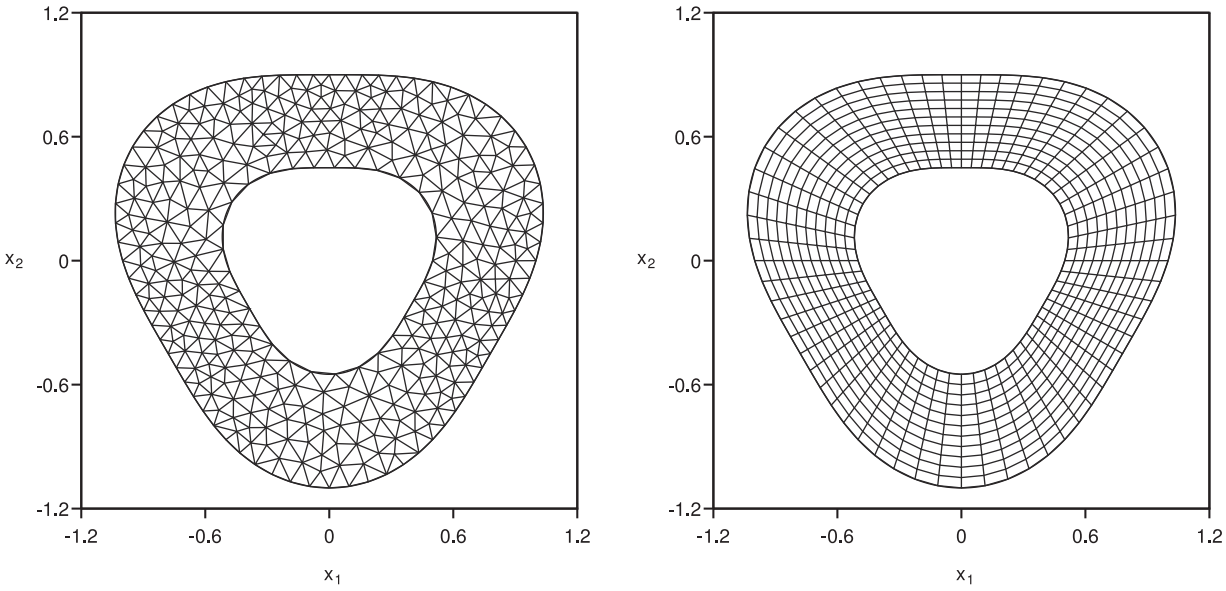

Fig. 9. Coarse uniform triangular Delaunay mesh (left panel) and uniform quadrilateral mesh (right panel) prescribed for the rose-shaped domain.

Table 4
Rose-shaped problem – Test 1 – Errors and convergence rates for the ROD2 method with uniform triangular Delaunay meshes.

	$\mathbb{P}_1$				$\mathbb{P}_3$				$\mathbb{P}_5$			
DOF	E_1	O_1	E_∞	O_∞	E_1	O_1	E_∞	O_∞	E_1	O_1	E_∞	O_∞
667	2.21E−02	–	4.91E−02	–	3.59E−04	–	3.56E−03	–	2.20E−04	–	1.52E−03	–
2590	6.23E−03	1.86	1.40E−02	1.85	1.85E−05	4.38	2.30E−04	4.04	2.77E−06	6.45	3.04E−05	5.77
10,274	1.48E−03	2.09	4.49E−03	1.65	1.17E−06	4.00	2.02E−05	3.53	5.58E−08	5.67	1.12E−06	4.79
41,367	3.29E−04	2.16	1.21E−03	1.88	9.17E−08	3.66	1.53E−06	3.71	7.02E−10	6.28	2.07E−08	5.73
165,599	6.96E−05	2.24	3.45E−04	1.81	6.58E−09	3.80	1.07E−07	3.83	1.37E−11	5.68	3.85E−10	5.74

Table 5
Rose-shaped problem – Test 1 – Errors and convergence rates for the ROD2 method with uniform quadrilateral meshes.

	$\mathbb{P}_1$				$\mathbb{P}_3$				$\mathbb{P}_5$			
DOF	E_1	O_1	E_∞	O_∞	E_1	O_1	E_∞	O_∞	E_1	O_1	E_∞	O_∞
660	6.42E−02	–	8.73E−02	–	1.41E−03	–	7.86E−03	–	9.75E−04	–	4.73E−03	–
2760	1.61E−02	1.93	2.23E−02	1.91	2.56E−04	2.39	8.45E−04	3.12	1.20E−05	6.15	8.33E−05	5.65
11,280	4.02E−03	1.97	5.60E−03	1.96	2.00E−05	3.62	8.48E−05	3.27	1.66E−07	6.08	1.08E−06	6.17
46,080	9.87E−04	2.00	1.38E−03	1.99	1.14E−06	4.07	5.93E−06	3.78	2.76E−09	5.83	2.00E−08	5.68
185,280	2.47E−04	1.99	3.45E−04	1.99	7.50E−08	3.91	3.84E−07	3.93	7.72E−11	5.14	3.42E−10	5.85

where (r, θ) are the polar coordinates and $R_{\mathrm{I}}(\theta;\alpha_{\mathrm{I}})$ and $R_{\mathrm{E}}(\theta;\alpha_{\mathrm{E}})$, $\alpha_{\mathrm{I}}, \alpha_{\mathrm{E}} \in \mathbb{R}$, are given by

$$R_{\mathrm{I}}(\theta;\alpha_{\mathrm{I}}) = r_{\mathrm{I}}\left(1 + \frac{1}{10}\sin(\alpha_{\mathrm{I}}\theta)\right) \qquad \text{and} \qquad R_{\mathrm{E}}(\theta;\alpha_{\mathrm{E}}) = r_{\mathrm{E}}\left(1 + \frac{1}{10}\sin(\alpha_{\mathrm{E}}\theta)\right).$$

The global mapping from the Rose-shaped domain onto the annulus then reads

$$\begin{bmatrix} y_1 \\ y_2 \end{bmatrix} \to \begin{bmatrix} x_1 \\ x_2 \end{bmatrix} = T(y_1, y_2) = \left(\frac{R_E - r}{R_E - R_I} R_{\mathrm{I}}(\theta;\alpha_{\mathrm{I}}) + \frac{r - R_I}{R_E - R_I} R_{\mathrm{E}}(\theta;\alpha_{\mathrm{E}})\right)\begin{bmatrix} \cos(\theta) \\ \sin(\theta) \end{bmatrix}.$$

The manufactured solution on the Rose-shaped domain is then given by

$$\psi(x_1, x_2) = \phi(T^{-1}(x_1, x_2)).$$

Notice that we recover the annulus geometry with $\alpha_{\mathrm{I}} = \alpha_{\mathrm{E}} = 0$. The associated source term f is obtained from Eq. (1) while homogeneous Dirichlet boundary condition still holds on the new boundaries Γ_{I} and Γ_{E}. All the simulations have been carried out with $\kappa = 1$ and $u = 1$.

First test. The transformation is parametrized with $\alpha_{\mathrm{I}} = 3$ and $\alpha_{\mathrm{E}} = 3$ and we plot in Fig. 8 the manufactured solution and the source term in the new domain.

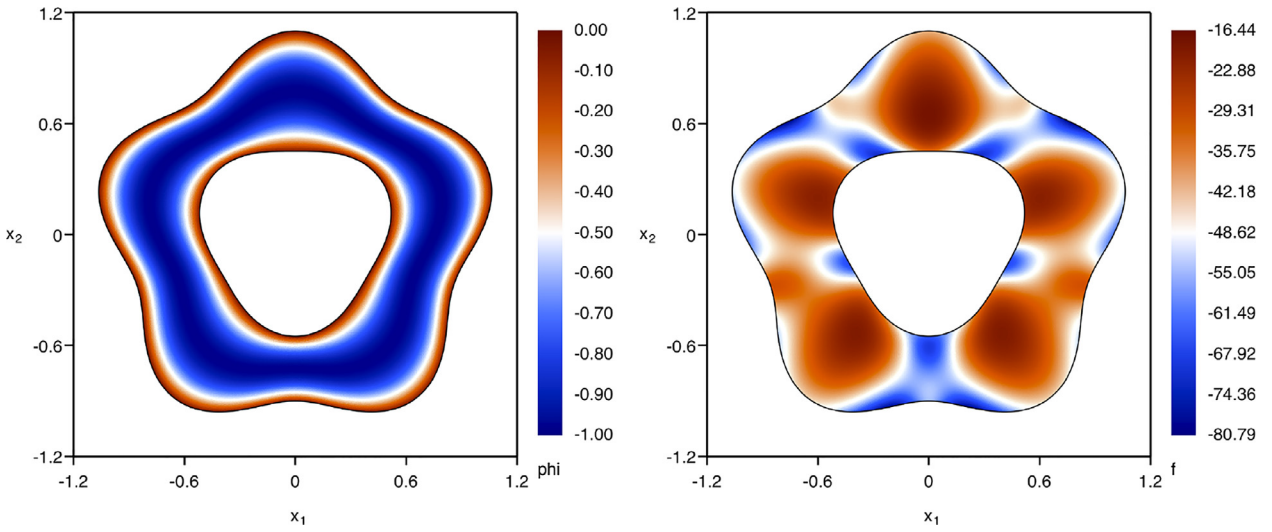

Fig. 10. Manufactured solution (left panel) and source term (right panel). (For interpretation of the colormap in this figure, the reader is referred to the web version of this article).

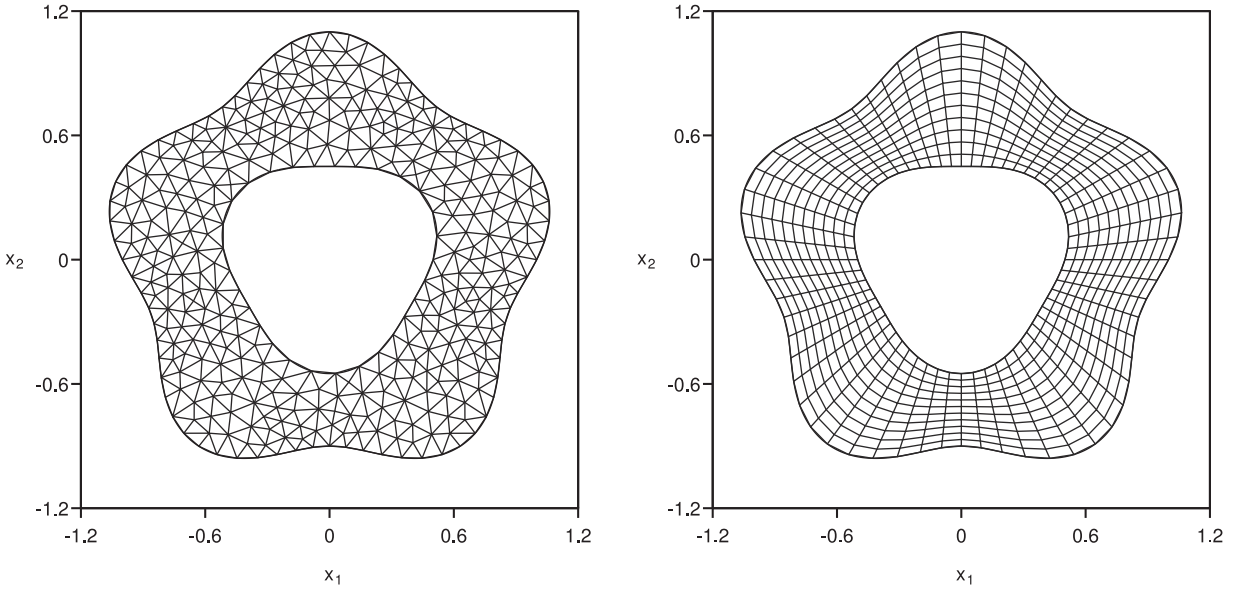

Fig. 11. Coarse uniform triangular Delaunay mesh (left panel) and uniform quadrilateral mesh (right panel) prescribed for the rose-shaped domain.

We carried out the simulations with successive refined regular triangular Delaunay meshes and also with quadrilateral meshes, see Fig. 9, to show the ability of the method to handle different cell shapes.

We report in Table 4 the errors and the convergence rates obtained with the ROD2 method (Delaunay meshes) while Table 5 reports the same informations for the quadrilateral meshes. We obtain the optimal convergence orders and no oscillation is reported. Computations have also been carried out with the second-order boundary approximation (not presented here) and we observe a second-order of convergence due to an inadequate treatment of the boundary condition.

Second test. The second test deals with a more wavy boundary setting $\alpha_I = 3$ and $\alpha_E = 5$. We plot in Fig. 10 the manufactured solution and the source term.

As in the previous case, simulations with successive refined regular Delaunay meshes or quadrilateral meshes have been carried out, see Fig. 11.

Table 6
Rose-shaped problem – Test 2 – Errors and convergence rates for the ROD2 method with uniform triangular Delaunay meshes.

	$\mathbb{P}_1$				$\mathbb{P}_3$				$\mathbb{P}_5$			
DOF	E_1	O_1	E_∞	O_∞	E_1	O_1	E_∞	O_∞	E_1	O_1	E_∞	O_∞
645	2.71E−02	–	6.97E−02	–	6.80E−04	–	8.76E−03	–	5.12E−04	–	5.86E−03	–
2550	7.56E−03	1.86	2.30E−02	1.61	4.49E−05	3.95	7.62E−04	3.55	1.29E−05	5.36	2.45E−04	4.62
10,244	1.89E−03	2.00	7.30E−03	1.65	3.71E−06	3.59	1.28E−04	2.57	2.98E−07	5.42	1.39E−05	4.12
40,789	4.10E−04	2.21	1.97E−03	1.89	2.53E−07	3.89	6.70E−06	4.27	9.53E−09	4.98	4.91E−07	4.84
162,011	9.63E−05	2.10	5.92E−04	1.75	1.89E−08	3.76	9.37E−07	2.85	1.20E−10	6.34	1.07E−08	5.55

Table 7
Rose-shaped problem – Test 2 – Errors and convergence rates for the ROD2 method with uniform quadrilateral meshes.

	$\mathbb{P}_1$				$\mathbb{P}_3$				$\mathbb{P}_5$			
DOF	E_1	O_1	E_∞	O_∞	E_1	O_1	E_∞	O_∞	E_1	O_1	E_∞	O_∞
660	6.91E−02	–	1.11E−01	–	5.06E−03	–	3.27E−02	–	5.37E−03	–	3.60E−02	–
2760	1.74E−02	1.93	2.85E−02	1.90	3.94E−04	3.57	3.57E−03	3.10	1.33E−04	5.17	1.61E−03	4.35
11,280	4.37E−03	1.96	7.13E−03	1.97	4.70E−05	3.02	3.83E−04	3.17	2.27E−06	5.78	5.07E−05	4.91
46,080	1.08E−03	1.99	1.77E−03	1.98	3.36E−06	3.75	2.50E−05	3.88	4.85E−08	5.47	1.07E−06	5.48
185,280	2.71E−04	1.99	4.42E−04	1.99	2.05E−07	4.02	1.57E−06	3.98	1.11E−09	5.42	1.41E−08	6.22

We report in Tables 6 and 7 the errors and the convergence rates obtained with the ROD2 method and we confirm the ability of the scheme to preserve the optimal order in function of the polynomial degree used for the reconstruction procedure.

7. Conclusions

We have presented a very high-order finite volume scheme to solve the steady-state bi-dimensional convection–diffusion problem based on a new class of polynomial reconstructions. Two approaches were proposed to overcome the second-order accuracy limitation when dealing with non-polygonal domain and Dirichlet boundary conditions. The first one consists in analytically constraining the boundary element reconstructions in order to satisfy the boundary condition at a point on the physical domain boundary. Such approach differs from the Olliver-Gooch and Van Altena approach in the sense that the flux calculation is performed on the straight edge and no curved element is necessary. The proposed ROD method consists in constraining the boundary reconstructions by *a posteriori* computing the associated free parameter such that the reconstructions satisfy appropriately the boundary condition. This procedure relies on the fact that the least-squares matrix associated to the reconstruction is decoupled from the boundary parameterization and, therefore, is less sensitive to the boundary location.

Several numerical tests considering simple and complex curved domains were simulated to observe that we achieve effective optimal order of accuracy both for structured and unstructured meshes for the two-dimensional linear steady-state convection–diffusion problem. A pure convection problem (hyperbolic scalar equation) was also tested and optimal order accuracy rates were achieved without any reported oscillations.

This work represents a proof of concept showing that very high-order of accuracy Finite Volume scheme on unstructured can handle curved boundary conditions at the optimal order of accuracy without the need for a boundary fitted mesh or complex transformations. For future works we plan to extend this approach to other boundary conditions (Neumann, Robin), to unsteady systems (Euler, Navier–Stokes) with time evolving domain (piston, pulsating interfaces, etc.). We also plan to investigate the extension of ROD to unstructured 3D mesh. Even if, conceptually speaking, the ROD method does not depend on the space dimension, the machinery needed in three-dimensional will demand delicate validation and verification.

Acknowledgments

This research was financed by FEDER Funds through Programa Operational Fatores de Competitividade – COMPETE and by Portuguese Funds FCT – Fundação para a Ciência e a Tecnologia, within the Strategic Project UID/MAT/00013/2013. R. L. and R. C. thank the financial support of the “International Centre for Mathematics and Computer Science in Toulouse” (CIMI) partially supported by ANR-11-LABX-0040-CIMI within the program ANR-11-IDEX-0002-02. The authors would also like to thank the referee for the additional informations and references.

References

[1] F. Bassi, S. Rebay, High-order accurate discontinuous finite element solution of the 2d Euler equations, J. Comput. Phys. 138 (2) (1997) 251–285.
[2] L. Krivodonova, M. Berger, High-order accurate implementation of solid wall boundary conditions in curved geometries, J. Comput. Phys. 211 (2006) 492–512.
[3] Z.J. Wang, High-order computational fluid dynamics tools for aircraft design, Philos. Trans. R. Soc. A 372 (2014) 20130318.

[4] Z.J. Wang, High-order methods for the euler and Navier–Stokes equations on unstructured grids, Prog. Aerosp. Sci. 43 (1–3) (2007) 1–41.
[5] D. Mavriplis, Results from the 3rd Drag Prediction Workshop Using the NSU3d Unstructured Mesh Solver, AIAA Paper 2007-256 (2007).
[6] I. Ergatoudis, B.M. Irons, O.C. Zienkiewicz, Curved, isoparametric, quadrilateral elements for finite element analysis, Int. J. Solids Struct. 4 (1968) 31–42.
[7] P.G. Ciarlet, P.A. Raviart, Interpolation over curved elements with applications to finite element methods, Comput. Methods Appl. Mech. Eng. 1 (1972) 217–249.
[8] M. Zlámal, Curved elements in the finite element method i, SIAM J. Numer. Anal. 10 (1973) 229–240.
[9] M. Zlámal, Curved elements in the finite element method II, SIAM J. Numer. Anal. 11 (1974) 347–368.
[10] B. Cockburn, G.E. Karniadakis, C.W. Shu, The development of discontinuous Galerkin methods, in: B. Cockburn, G.E. Karniadakis, C.-W. Shu (Eds.), Discontinuous Galerkin Methods. Theory, Computation and Applications, 11, Springer Verlag, Berlin, Heidelberg, 2000, pp. 5–50. Lecture Notes in Computational Sicence and Engineering.
[11] F. Hindenlang, T. Bolemann, C.D. Munz, Mesh curving techniques for high order discontinuous Galerkin simulations, in: N. Kroll, C. Hirsch, F. Bassi, C. Johnston, K. Hillewaert (Eds.), Industrialization of High-Order Methods – A Top-Down Approach, 128, Springer International Publishing, 2015, pp. 133–152.
[12] Z.J. Wang, Y. Liu, Extension of the spectral volume method to high-order boundary representation, J. Comput. Phys. 211 (2006) 154–178.
[13] W.J. Gordon, C.A. Hall, Construction of curvilinear co-ordinate systems and applications to mesh generation, Int. J. Numer. Methods Eng. 7 (4) (1973) 461–477.
[14] W.J. Gordon, C.A. Hall, Transfinite element methods: blending-function interpolation over arbitrary curved element domains, Numer. Math. 21 (2) (1973) 109–129.
[15] C. Geuzaine, J.F. Remacle, Gmsh: a three-dimensional finite element mesh generator with built-in pre- and post-processing facilities, Int. J. Numer. Methods Eng. 79 (2009) 1309–1331.
[16] N. Balakrishnan, G. Fernandez, Wall boundary conditions for inviscid compressible flows on unstructured meshes, Int. J. Numer. Methods Fluids 28 (1998) 1481–1501.
[17] B. Cockburn, M. Solano, Solving dirichlet boundary-value problems on curved domains by extensions from subdomains, SIAM J. Sci. Comput. 34 (2012) 497–519.
[18] B. Cockburn, M. Solano, Solving convection–diffusion problems on curved domains by extensions from subdomains, J. Sci. Comput. 59 (2014) 512–543.
[19] W. Qiu, M. Solano, P. Vega, A high order HDG method for curved-interface problems via approximations from straight triangulations, J. Sci. Comput. 69 (2016) 1384–1407.
[20] E. Burman, S. Claus, P. Hansbo, M.G. Larson, A. Massing, CutFEM: discretizing geometry and partial differential equations, Int. J. Numer. Methods Eng. 104 (2015) 472–501.
[21] C. Lehrenfeld, A. Reusken, Analysis of a high order unfitted finite element method for an elliptic interface problem, IMA J. Numer. Anal. (2017), doi:10.1093/imanum/drx041. (accessed 28.09.2017).
[22] C. Lehrenfeld, High order unfitted finite element methods on level set domains using isoparametric mappings, Comput. Methods Appl. Mech. Eng. 300 (2016) 716–733.
[23] C. Ollivier-Gooch, M.V. Altena, A high-order-accurate unstructured mesh finite-volume scheme for the advection-diffusion equation, J. Comput. Phys. 181 (2) (2002) 729–752.
[24] C. Michalak, C. Ollivier-Gooch, Unstructured High-order Accurate Finite Volume Solutions of the Navier–Stokes Equations, AIAA Paper 2009-954 (2009).
[25] C. Ollivier-Gooch, A. Nejat, C. Michalak, On Obtaining High-order Finite-volume Solutions to the Euler Equations on Unstructured Meshes, AIAA Paper 2007-4464 (2007).
[26] C. Ollivier-Gooch, A. Nejat, C. Michalak, On obtaining and verifying high-order unstructured finite volume solutions to the euler equations, AIAA J. 47 (9) (2009) 2105–2120.
[27] A. Boularas, S. Clain, F. Baudoin, A sixth-order finite volume method for diffusion problem with curved boundaries, Appl. Math. Model. 41 (2017) 401–422.
[28] T.J. Barth, P.O. Frederickson, Higher Order Solution of the Euler Equations on Unstructured Grids Using Quadratic Reconstruction, AIAA Paper 90-0013 (1990).
[29] T.J. Barth, Recent Developments in High Order k-exact Reconstruction on Unstructured Meshes, AIAA Paper 93-0668 (1993).
[30] S. Clain, G.J. Machado, J.M. Nóbrega, R.M.S. Pereira, A sixth-order finite volume method for the convection–diffusion problem with discontinuous coefficients, Comput. Methods Appl. Mech. Eng. 267 (2013) 43–64.
[31] A. Ern, J.L. Guermond, Theory and Practice of Finite Elements, 159, Springer Verlag, New-York, 2004.